



Superior performance of anion exchange membrane water electrolyzer: Ensemble of producing oxygen vacancies and controlling mass transfer resistance

Yoo Sei Park^{a,b,1}, Juchan Yang^{a,1}, Jongmin Lee^c, Myeong Je Jang^a, Jaehoon Jeong^a, Woo-Sung Choi^a, Yangdo Kim^b, Yadong Yin^d, Min Ho Seo^{c,*}, Zhongwei Chen^{e,*}, Sung Mook Choi^{a,*}

^a Materials Center for Energy Department, Surface Technology Division, Korea Institute of Materials Science, Changwon, 642831, Republic of Korea

^b Department of Materials Science and Engineering, Pusan National University, Busan, 46241, Republic of Korea

^c Fuel Cell Research and Demonstration Center, Future Energy Research Division, Korea Institute of Energy Research, Buan-gun, 56332, Republic of Korea

^d Department of Chemistry, Materials Science and Engineering Program and UCR Center for Catalysis, University of California Riverside, CA, 92521, USA

^e Department of Chemical Engineering, University of Waterloo, Waterloo, Ontario, N2L 3G1, Canada

ARTICLE INFO

Keywords:

Electrocatalyst
Oxygen vacancy
Oxygen evolution
Hydrogen energy
Anion exchange membrane water electrolysis

ABSTRACT

A chemically etched CuCo-oxide (CE-CCO) electrode prepared by electrodeposition was used for oxygen evolution reaction electrocatalyst. Surface chemical etching of CuCo-oxide (CCO) introduced oxygen vacancies and thus increased electrical conductivity to promote oxygen generation. During practical applicability testing, when CE-CCO was used as the anode of an anion-exchange membrane water electrolyzer, enhanced oxygen evolution performance was observed (current density = 1390 mA/cm² at 1.8 V_{cell}), which, among other reactions, was ascribed to the easy removal of O₂ from the aerophobic electrode surface. In addition to featuring low mass transfer resistance even at high current density with substantial gas generation, the CE-CCO electrode featured remarkable durability, exhibiting stable performance over 3600 h under the conditions of continuous O₂ evolution. Thus, this work shows that the performance of electrodeposited oxide catalysts can be enhanced by introducing oxygen vacancies, while the energy conversion efficiency of the corresponding water electrolysis systems can be increased by lowering mass transfer resistance via efficient gas removal and reactant supply.

1. Introduction

Hydrogen is a renewable and sustainable energy source with its high energy density and no carbon emission. Today, hydrogen is largely produced by petrochemical processes such as the steam reforming of natural gas, gasification, and partial oxidation [1]. However, these processes inevitably release greenhouse gases into the atmosphere, which reduces the advantages of hydrogen energy. As a result, there have been many studies on the development of proton exchange membrane water electrolysis (PEMWE) system [1,2] and alkaline water electrolysis (AWE) system [3–5], which can produce high purity hydrogen without any greenhouse gas emissions. Although the latter systems feature the advantages of high technology intensity, easy handling, and cost-effectiveness (due to use of non-precious metal catalysts), they employ liquid electrolytes and therefore suffer from the

leakage of electrolyte, corrosion problem and low energy density. PEMWE systems exhibit high rates of hydrogen production together with high technological maturity, and are currently being commercialized. However, as these systems are operated under acidic conditions, the scope of oxygen evolution reaction (OER) electrocatalysts is limited to expensive noble metal oxides such as RuO₂ and IrO₂, which places a certain limit on the reduction of hydrogen production costs [6]. To address these challenges, new anion-exchange membrane water electrolysis (AEMWE) systems combining the advantages of the above two platforms have been developed [7–10]. These systems can produce high-purity hydrogen using anion exchange membrane as the solid electrolyte, similarly to PEMWEs, and are operated in an alkaline environment, which allows them to employ inexpensive non-noble-metal catalysts [9]. Still, the performance of AEMWE systems is much lower than that of PEMWE ones because of the poor OER performance of non-

* Corresponding authors.

E-mail addresses: foifrit@kier.re.kr (M.H. Seo), zhwchen@uwaterloo.ca (Z. Chen), akyzaky@kims.re.kr (S.M. Choi).

¹ These authors have contributed equally.

precious-metal electrocatalysts. Therefore, many studies have been conducted on the development of non-precious-metal electrocatalysts with good OER performance so that the AEMWE system performance can approach the performance of the PEMWE systems.

The ultimate goal of developing non-precious-metal electrocatalysts for water electrolysis is the realization of large-scale cost-effective hydrogen production, which requires the use of high current densities ($\geq 500 \text{ mA/cm}^2$ at 1.8–2.4 V) [11,12]. Importantly, both lab-scale and commercial-device (e.g., PEMWE and AEMWE) performance under actual operation conditions should be guaranteed. In commercial water splitting systems, the production of H_2 at the cathode is obstructed because of the slow kinetics of the OER ($4\text{OH}^- \rightarrow \text{O}_2 + 2\text{H}_2\text{O} + 4\text{e}^-$) at the anode [13]. Despite the importance of the OER, the high overpotential of OER acts as a bottleneck and decreases water splitting efficiency. Therefore, highly efficient OER electrocatalysts should be developed to improve the energy efficiency of water splitting.

Numerous non-precious-metal OER electrocatalysts with excellent activity have been reported, e.g., transition metal sulfides [14–17]/phosphides [11,18,19]/oxides [20–22] and layered double hydroxide [23–25]. The very low overpotentials ($\leq 300 \text{ mV}$ at 10 mA/cm^2) and superior durability of these catalysts are expected to aid the commercialization of water electrolyzers. However, most related studies do not report the performance of these catalysts in commercial devices, as it is affected by parameters such as the conditions of membrane electrode assembly (MEA) fabrication, cell operation temperature, electrolyte flow rate, and cell fabrication pressure [7,9,26,27]. Above all, the high performance of a given catalyst in a laboratory setting does not guarantee the high performance of the corresponding commercial device [8]. Therefore, both lab-scale and commercial-device performances of electrocatalysts should be reported for a complete picture.

Traditionally, electrocatalysts have been synthesized in the form of powders, which places certain limitations on the electrode fabrication process, and hence, on electrode performance [7,26]. Electrode fabrication can be described by numerous parameters such as slurry composition (solvent, catalyst, and binder) and coating method [2,7,28]. In addition, electrodes are typically subjected to heat treatment or high-temperature pressing [7,26]. As the broad range of variables complicates the optimization of the electrode fabrication process, simple techniques of high-performance electrode fabrication are highly sought after. Electrodeposition is one of such techniques, featuring the direct deposition of electrocatalysts on a conductive substrate and thus allowing one to avoid the optimization of electrode fabrication conditions, which means that the performance of electrodeposited catalysts in commercial devices is guaranteed [19,29]. Moreover, electrodeposited catalysts exhibit excellent electrical conductivity with lower ohmic contact resistance between the electrodeposited catalyst layer and the substrate than conventional powder-type catalysts mixed with polymeric binders such as polytetrafluoroethylene and ionomers to prevent catalyst detachment [30,31]. Additionally, as electrocatalysts are directly grown on the substrate electrode, they are strongly bonded to the same and exhibit high mechanical strength. The compositional and morphological changes of electrocatalysts can be easily controlled by change of electrolyte composition, electrodeposition time, and potential [10,22,29,32]. As catalytic reactions occur on the surface, large surface areas benefit catalyst performance. Control of electrodeposition conditions allows one to produce large-surface-area structures such as nanosheets, nanodendrites, and nanoparticles. Finally, electrodeposition-fabricated electrodes have an advantageous structure allowing for the quick escape of oxygen generated at the anode due to low catalyst layer thickness [2,33]. Therefore, mass transfer losses (η_{mass}) at various overpotentials, e.g., ohmic (η_{ohm}) and kinetic (η_{kin}) losses, observed during water decomposition can be greatly reduced to decrease the total overpotential in AEMWE systems.

Herein, a hierarchically structured CuCo-oxide (CCO) OER electrocatalyst is prepared via electrochemical co-precipitation of Cu and Co hydroxides onto Ni foam (NF) followed by surface chemical etching and

annealing, and chemically etched CuCo-oxide (CE-CCO)/NF is directly used as an OER electrode. Furthermore, we not only probe the characteristics of the above electrocatalyst but also report its performance in a model commercial AEMWE system. The CE-CCO/NF electrode is shown to exhibit remarkable catalytic activity and stability for the OER (310 mV at 100 mA/cm^2 ; operation time = 3600 h) in a half-cell test, additionally featuring exceptional OER performance (1390 mA at $1.8 V_{\text{cell}}$) in an AEMWE system.

2. Experimental

2.1. Preparation of CE-CCO

The CE-CCO electrode was prepared by electrodeposition in a solution (50 mL) containing $\text{Co}(\text{NO}_3)_2 \cdot 6\text{H}_2\text{O}$ (50 mM) and $\text{Cu}(\text{NO}_3)_2 \cdot 2.5\text{H}_2\text{O}$ (15 mM), with nickel foam (NF) used as the working electrode substrate. Prior to electrodeposition, NF was etched with 5 M HCl for 30 min to remove surface oxide layers. A Pt mesh ($3 \text{ cm} \times 4 \text{ cm}$) and a saturated calomel electrode (SCE) separated by a distance of 1 cm were used as counter and reference electrodes, respectively. $(\text{Cu,Co})(\text{OH})_2$ was electrodeposited on NF (working area = 0.49 cm^2 for half-cell test, 7.4 cm^2 for AEMWE) at a constant potential of $-1 V_{\text{SCE}}$ (versus SCE) for 5 min at 30°C without stirring, and the obtained electrode was thoroughly rinsed with deionized water, immersed into 0.2 M ammonium persulfate (APS) for several seconds, and then rinsed several times with deionized water. The sample was then air-dried and heated to 250°C for 3 h at 1°C/min . This electrocatalyst was named as CE-CCO and the loading amount of CE-CCO in NF was about 3.8 mg/cm^2 . To compare the chemical etching effect, the CuCo oxide (CCO) was synthesized with the same way used for making CE-CCO mentioned above except of chemical etching process.

2.2. Physical property characterization

Sample morphologies and compositions were analyzed by field-emission scanning electron microscope (JSM-7001 F, JEOL, Japan) coupled with energy-dispersive X-ray spectrometry. X-ray diffraction patterns were recorded on an X-ray diffractometer (D/MAX 2500, Rigaku, Tokyo, Japan) for $2\theta = 20\text{--}80^\circ$ at a scan speed of $1^\circ/\text{min}$ using $\text{Cu K}\alpha$ radiation. XPS measurements were performed on a K-alpha (ThermoFisher Scientific, Waltham, MA) spectrometer, and high-resolution transmission electron microscope (HRTEM) images and SAED patterns were recorded on an JEM-2100 F (JEOL, Tokyo, Japan).

2.3. Electrochemical characterization

Electrochemical measurements were performed using a potentiostat (VMP-3, Biologic) in a three-electrode cell with 1 M KOH as an electrolyte at room temperature. A Pt mesh ($3 \text{ cm} \times 4 \text{ cm}$) was used as a counter electrode, and Hg/HgO (1 M KOH) was used as a reference electrode. All potentials were referenced to the RHE using the Nernst equation ($E_{\text{RHE}} (\text{V}) = E_{\text{Hg/HgO}} + 0.106 + 0.059 \text{ pH}$). The value of 0.106 V is the difference between the Hg/HgO (1 M KOH) electrode and the RHE under the chosen laboratory conditions. Although the ideal potential of the Hg/HgO (1 M KOH) electrode is 0.098 V, it was calculated as 0.106 V for accurate testing. N_2 -saturated 1 M KOH was used as an electrolyte for the OER test. OER activity was investigated by linear sweep voltammetry (LSV) at a rate of 5 mV/s. Electrochemical surface areas (ECSAs) was calculated from double layer capacitance (C_{dl}) using cyclic voltammetry (CV) measurements at scan rates of 5–80 mV/s in the non-faradaic region in 1 M KOH: $\text{ECSA} = C_{\text{dl}}/C_s$, where $C_s = 40 \mu\text{F/cm}^2$ is the smooth-plane capacitance of a metal surface. Stability was investigated at a constant current density of 20 mA/cm^2 for 3600 h. All electrochemical results were obtained using an iR compensation of 85 %. For comparison, commercially IrO_2 powders (Sigma Aldrich, 99.9 % trace metal basis) were tested by

droplet of the catalyst ink placed on Ni foam with same size of CE-CCO.

2.4. AEMWE single cell fabrication

The AEMWE system comprised the anode (CuCo-oxide on nickel foam, 7.4 cm²), cathode (1 mg/cm² of Pt/C (40 wt.%, HISPEC 4000, Johnson Matthey) on carbon cloth (Toray), 4.9 cm²), gas diffusion layer (NF, Alantum, pore size: 450 μm), and anion exchange membrane (AEM, X37-50 Grade T, Dioxide Materials), as shown in Fig. 6a. IrO₂ powder (Sigma Aldrich) was used as an anode catalyst for comparison with precious metal oxides and loaded on NF with PTFE. The loading amount of IrO₂ was 4 mg/cm². The single cell was supplied with 1 M KOH as an electrolyte at 24 mL/min and was operated at 45 °C. The AEMWE test was performed using a potentiostat (BP2C, ZIVE LAB), and electrochemical performance was analyzed by constant-potential and LSV (from 1.4 to 1.9 V_{cell}) measurements. The long-term testing of AEMWE systems was conducted at 500 mA/cm² for 64 h. Energetic efficiency of the AEMWE was calculated by the following equation.

$$\eta = \frac{E_{\text{Output}}}{E_{\text{Input}}} = \frac{V_{\text{H}_2} \cdot H_0}{W_{\text{H}}} \times 100 \quad (1)$$

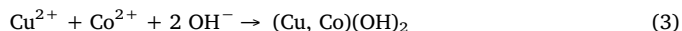
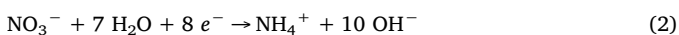
Wh is the electric power to produce hydrogen, H₀ is the calorific value of hydrogen (10.8 × 10⁶ J/m³, lower heating value) and V_{H₂} is the hydrogen gas volume.

2.5. Computational details

DFT calculations was performed using the Vienna ab initio Simulation Package [34]. The projector augmented wave pseudopotential was used to replace the interaction of core electrons [35,36]. Electron exchange-correlation energies were calculated using Perdew-Burke-Ernzerhof functionals and the generalized gradient approximation [37,38]. Kohn-Sham wave functions of valence electrons were expanded using a plane wave basis set with an energy cut-off of 520 eV. In addition, the Hubbard U parameter (GGA + U) was employed to improve the description of correlation effects and reduce the self-interaction error [39–41]. The Methfessel-Paxton smearing method was implemented [42]. Optimized effective interaction parameters U_{eff} (U_{eff} = U – J) of 3.4 and 4 eV were used for Co and Cu, respectively, in CuCo₅O₈ and CuCo₅O₇. The total energy for the ionic relaxation step was controlled within 1 × 10⁻⁴ eV. A gamma point mesh with (21 × 21 × 21) k-points was used for CuCo₅O₈ and CuCo₅O₇ unit cells to sample the Brillouin zone for bulk calculations. After the geometric optimization of bulk CuCo₅O₈ and CuCo₅O₇, slab models were designed and calculated in terms of the (110) surface direction with a (6 × 6 × 1) k-point mesh for a (1 × 1) surface unit cell and with smaller meshes for larger supercells. A vacuum space of 30 Å was employed to avoid interactions between top and bottom surfaces. After each crystal surface energy was calculated, oxygen-containing intermediates (O, OH, OOH and O₂) were deposited on the (110) surfaces of CuCo₅O₈ and CuCo₅O₇ to draw the free energy diagram. To simulate the effect of solvation by water, point charges were added in the vacuum slab using the implicitly implemented method of VASPsol [43]. Finally, the charge density difference between CuCo₅O₈ (110) and CuCo₅O₇ (110) facets was calculated by Bader charge analysis [44].

3. Results and discussion

The CE-CCO electrode was electrodeposited using a modification of a previously reported method (Fig. 1) [22]. Specifically, a mixture of Cu and Co hydroxide nanosheet arrays was electrodeposited on NF, with the equations describing the electrodeposition process given below [29].



At the onset of electrodeposition, NO₃⁻ was reduced to NH₄⁺ and OH⁻. The latter anions reacted with Cu (II) and Co (II) ions to afford a precipitate of (Cu,Co)(OH)₂ (CCHO) nanosheets with a honeycomb morphology and a thickness of 20–30 nm on NF (Fig. 1). The CCHO-deposited on NF was then immersed into 0.2 M ammonium persulfate (APS) for several seconds, which resulted in oxidation of the CCHO surface and, hence, in a change from a nanosheet array to crumbled nanosheets. The surface morphology was not changed after annealing. The thickness of CCO was ~2.9 μm (Fig. S1), whereas that of CE-CCO was lower (2.2 μm) because of chemical etching (Fig. S2).

Further structural characterization of CCO/CE-CCO was performed by high-resolution transmission electron microscopy (TEM; Figs. 2a, c and S3), and the corresponding selected-area electron diffraction (SAED) patterns revealed the presence of a spinel-type polycrystalline Co₃O₄ structure. However, the similarity of unit cell parameters did not allow Co₃O₄ to be distinguished from CCO/CE-CCO [a = b = c = 8.065 Å for Co₃O₄ and a = b = c = 8.140 Å for CuCo₂O₄]. EDS mapping revealed the presence of Cu, Co, and O in the nanostructures and demonstrated that all CCO and CE-CCO components were uniformly distributed (Fig. 2b, d). In particular, intensive distribution of Cu in CCO and CE-CCO was observed, and the corresponding region was presumed to be CuO. X-ray diffraction (XRD) analysis (Fig. 2e) showed that CCO and CE-CCO contained CuO (JCPDS: 00-005-0661) and Cu_{0.75}Co_{2.05}O₄ (JCPDS: 01-078-2176). Notably, CE-CCO showed low crystallinity, as indicated by peak broadening because of etching effect. The decreased peak intensity and increased peak width indicate smaller crystallites and higher structural disorders in CE-CCO [45]. Peaks at 44.6°, 51.9°, and 76.8° corresponded to metallic Ni (JCPDS: 00-001-1260) from NF. As the OER mainly occurs on the electrocatalyst surface, we probed the surface electronic properties of CCO and CE-CCO by X-ray photoelectron spectroscopy (XPS), and the corresponding survey spectra (Fig. S4) indicated the presence of Cu, Co, and O. Fig. 3(a–d) present high-resolution Cu 2p, Co 2p, and O 1s spectra, revealing the presence of Co 2p_{3/2} and Co 2p_{1/2} peaks at 780 and 795 eV, for both CCO and CE-CCO, respectively [46–48].

Compared to that of CCO, the Co 2p spectrum of CE-CCO featured higher-intensity satellite peaks at 785.58 and 803.28 eV, which indicated an increased content of Co²⁺ due to the partial reduction of Co³⁺. According to a previous report [46,49,50], the Co²⁺/Co³⁺ ratio is positively correlated with the concentration of oxygen vacancies. To confirm this suggestion, we calculated the above ratios from the integrated areas of Co 2p peaks and the relative sensitivity factor as 0.76 and 1.55 for CCO and CE-CCO, respectively. Thus, CE-CCO had a higher concentration of surface oxygen vacancies than CCO. To gain further insights, O 1s spectra were deconvoluted into peaks of chemisorbed water (O_W: ~532.5 eV), oxygen vacancies (O_V: ~531.8 eV), hydroxyls (O_{OH}: ~531 eV) and lattice oxygen (O_L: ~530 eV), as shown in Fig. 3b [21,50]. Compared to CCO, CE-CCO featured a more intense O_V signal, which, together with the results above, indicated that the Co²⁺/Co³⁺ ratio was positively correlated with surface oxygen vacancy concentration (Fig. 3c).

Investigation of the relationship between oxygen vacancy and electrocatalytic effect suggests that the introduction of oxygen vacancies into Co₃O₄ changes the adsorption energy of H₂O molecules at active sites to enhance OER performance [51]. The impact of this factors on electrocatalytic effects is discussed below. As shown in Fig. 3d, the two main peak at binding energies of ~934 eV (Cu2p_{3/2}) and ~954 eV (Cu2p_{1/2}) could be deconvoluted into four peak components, and these could be best fitted to the spinel oxide of Cu¹⁺ and Cu²⁺ [22].

The relationship between local-structure oxygen vacancies and Co oxidation states in CCO and CE-CCO was probed by X-ray absorption near-edge structure (XANES) and extended X-ray absorption fine structure (EXAFS) measurements. As shown in Fig. 3e, the Co K-edge of

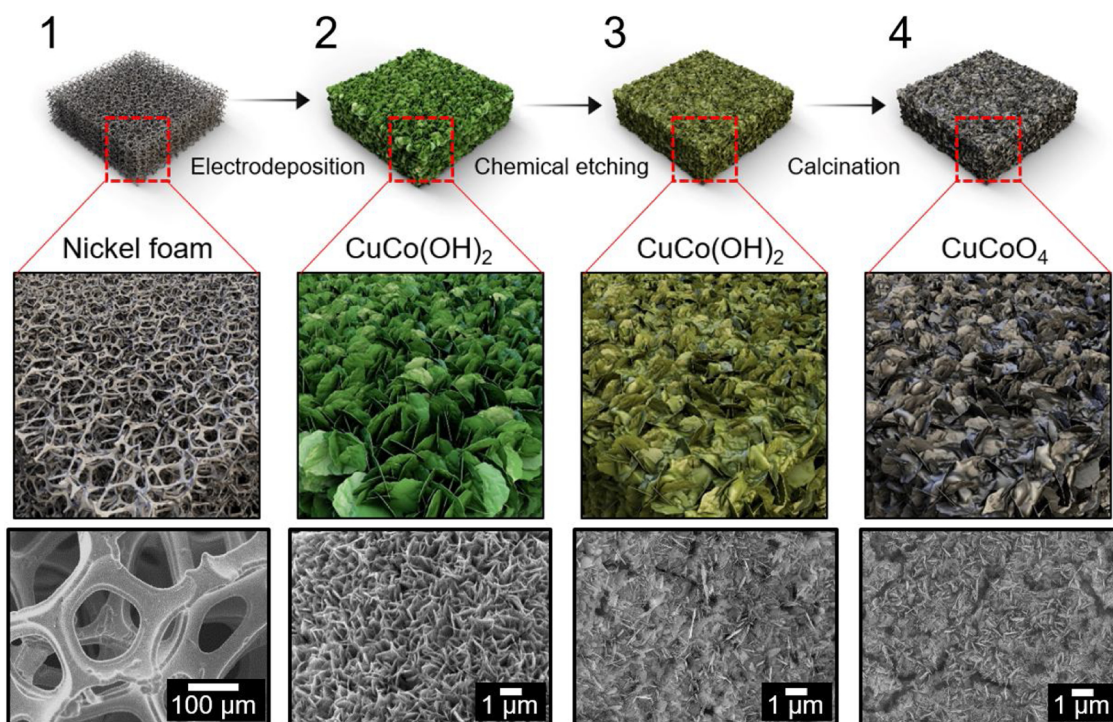


Fig. 1. Schematic illustration depicting the synthesis of the chemical etched CuCoO₄ anode in this work. (1) Panel represent the nickel foam (NF) substrate, which was used 3D-support electrode. (2) The CuCo(OH)₂ was deposited on NF by electrodeposition. (3) Surface of CuCo(OH)₂ was chemical etched by ammonium persulfate (APS). (4) CuCoO₄ was converted from CuCo(OH)₂ by calcination.

CCO was shifted to lower energy in the CE-CCO, which was attributed to the lower Co oxidation state due to oxygen vacancy presence [52]. Moreover, the presence of oxygen vacancies was confirmed by EXAFS-based observation of Co local structure (Fig. 3f). The first peak corresponded to Co–O distances in tetrahedral (Co²⁺–O) and octahedral (Co³⁺–O) settings, and the second peak corresponded to the Co–Co distance between two octahedral units (Co³⁺–Co³⁺) [18]. The Co–O bonds of CE-CCO were shorter than those of CCO, in agreement with the presence of oxygen vacancies [53].

The electrochemical behavior of NF, CE-CCO, and IrO₂ electrodes in an alkaline medium was investigated by linear sweep voltammetry (LSV) (Fig. 4a). The CE-CCO electrode was compared to that comprising commercial IrO₂, which is one of the best OER electrocatalysts available to date. Although CE-CCO showed a higher onset potential than IrO₂ at higher potentials, the current density of CE-CCO exponentially increased to a greater extent than in the case of IrO₂. Compared to IrO₂, which had an overpotential of 379 mV at 100 mA/cm², CE-CCO featured a lower overpotential. Moreover, compared to CCO, CE-CCO exhibited higher catalytic activity and an exceptionally low OER overpotential of 310 mV at 100 mA/cm² (Fig. S5). Electrocatalytic activity was further assessed by comparison of Tafel slopes (Fig. S6) and overpotentials at 100 mA/cm² (Fig. 4b). The Tafel slopes of NF, IrO₂, CCO, and CE-CCO approximately equaled 70 mV/dec, in agreement with literature. Notably, a Tafel slope of 60 mV/dec corresponds to the chemical RDS of the OER after the first electron-transfer step [54,55]. Electrochemical surface areas (ECSAs) were represented by double-layer capacitance (C_{dl}) determined from cyclic voltammetry (CV) curves recorded at different scan rates in the non-faradaic region (Fig. S7) [56]. The lowest (1.44 mF/cm²) and highest (5.57 mF/cm²) C_{dl} values were observed for NF and CCO, respectively. The reduced ECSA of CE-CCO was ascribed to the destruction of the large-surface-area nanosheet structure by surface oxidation before calcination. Fig. S8 shows normalized polarization curves used to calculate current density per unit ECSA, revealing that the overpotentials required to achieve 1 mA/cm²_{ECSA} equaled 337 and 318 mV for CCO and CE-CCO,

respectively. Thus, CE-CCO had a larger activity per unit ECSA than CCO. To investigate the intrinsic catalytic properties of CCO and CE-CCO, we calculated the exchange current density (*j*₀) from Tafel plots (Fig. S9), showing that the *j*₀ of CE-CCO (2.77 × 10^{−3} mA/cm²) exceeded that of CCO (1.98 × 10^{−3} mA/cm²). After normalization with respect to ECSA, CE-CCO still had a larger *j*₀ than CCO (Table S1) [7]. Therefore, we concluded that oxygen vacancy generation during chemical etching improved the intrinsic catalytic properties of CCO for the OER. Among the factors determining catalyst performance, stability is as important as catalytic activity. Hence, CE-CCO stability was probed by conducting an oxygen generation experiment at a constant current density of 20 mA/cm² for 3600 h (~5 months; Fig. 4c). During the stability test, the electrolyte (1 M KOH) was replaced several times with a fresh solution, with the replacement date marked by a dotted line. The inset graph shows the fluctuation of overpotential due to the generation of oxygen gas and its removal from the electrode surface. To deliver a current density of 20 mA/cm² without iR compensation, an overpotential of 294 mV was required. During the test, a sudden overpotential increase due to electrolyte evaporation was observed. After 3600 h, the overpotential at 20 mA/cm² increased from 294 to 375 mV, i.e., 72.4 % of the initial performance was maintained. SEM imaging of fresh and durability-tested CE-CCO (Fig. 4d) revealed that testing induced some surface morphology changes, even though the catalytic properties of CE-CCO were relatively well maintained. Also, comparison of polarization curves before/after OER stability testing (Fig. S10) showed that CE-CCO retained its excellent activity after 3600 h. XRD analysis revealed that the chemical composition of durability-tested CE-CCO corresponded to Cu_{0.15}Co_{2.85}O₄ (JCPDS: 78-2172), which reflected Cu dissolution during testing (Fig. S11).

Next, CuCo₅O₈ (e.g., CCO) and CuCo₅O₇ (e.g., CE-CCO) were characterized by first-principle density functional theory (DFT) calculations to understand the origin of OER activity. The CuCo₅O₈ model was designed based on Co₃O₄ in the Inorganic Crystal Structure Database (ICSD) [57]. To explain the thermodynamically stable structures, we considered every configuration to define Cu and O vacancy

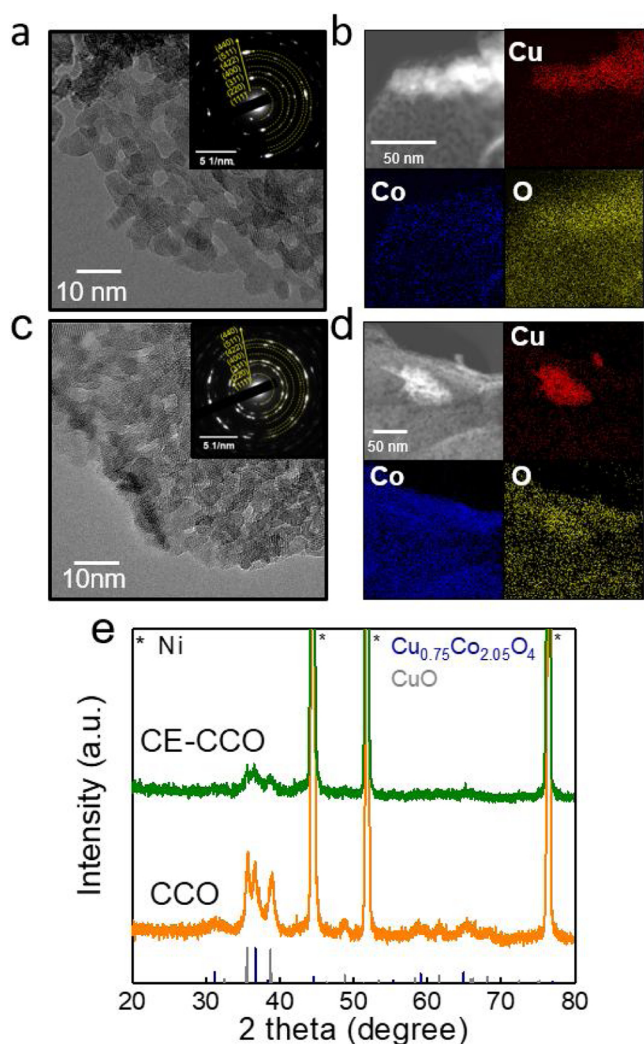


Fig. 2. Physical characterization of the CCO and CE-CCO anode. (a) High resolution-transmission electron microscopy images of CCO and inset show SAED ring pattern of CCO. (b) EDS mapping of Cu (red) / Co (blue) / O (yellow) in CCO. (c) HR-TEM images of CE-CCO and inset show SAED ring pattern of CE-CCO. (d) EDS mapping of Cu (red) / Co (blue) / O (yellow) in CE-CCO. (e) X-ray diffraction patterns of the CCO (orange line) and CE-CCO (green line) with reference patterns ($\text{Cu}_{0.75}\text{Co}_{2.05}\text{O}_4$; royal blue, CuO: grey). (For interpretation of the references to colour in this figure legend, the reader is referred to the web version of this article.)

sites in the crystal lattice of Co_6O_8 using a cluster expansion code [58,59]. After geometry relaxation of all generated structures, the most thermodynamically stable one with the lowest ground-state energy was selected.

Fig. S12 presents the simulated XRD patterns of CuCo_5O_8 and CuCo_5O_7 , showing that peaks of metal oxides with and without oxygen vacancies appeared at almost identical angles, i.e., no marked position shift due to vacancy presence was observed. The lattice parameters of CuCo_5O_8 and CuCo_5O_7 were very similar, in agreement with the experimental patterns of Fig. 2(e).

Further insights into the surface reactions for the OER were obtained by constructing (111), (110), and (100) slab models of CuCo_5O_8 to determine the lowest-surface-energy structure, which was found to be the (110) one. Then, the CuCo_5O_7 (110) slab model was defined after removal of oxygen at vacancy sites investigated for the CuCo_5O_7 bulk structure. To understand the electronic structure of metal oxides, we calculated the atomic partial charges for CuCo_5O_8 and CuCo_5O_7 slab models using Bader charge analysis [44]. The difference in charge

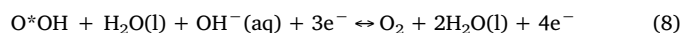
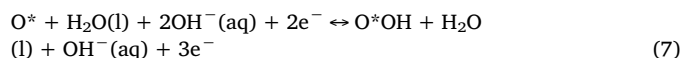
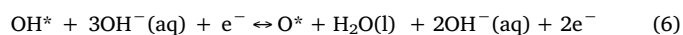
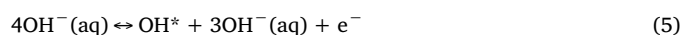
density was defined as shown in Eq. (4).

$$\rho = \rho_{\text{CuCoO}} - \rho_{\text{Cu}} - \rho_{\text{Co}} - \rho_{\text{O}} \quad (4)$$

Fig. 5(a, b) presents charge densities for CuCo_5O_8 (110) and CuCo_5O_7 (110) z-axes, with light pink regions around Co corresponding to the accumulation of positive charge, and spring green areas around O representing the depletion of negative charge. The introduction of oxygen vacancies changed the electronic structure of Co on the CuCo_5O_7 (110) surface, decreasing the oxidation state of Co in the bulk layer, with corresponding charge differences determined as $+1.31 e$ for CuCo_5O_8 and $+1.18 e$ for CuCo_5O_7 . In contrast, the charge differences of Co on the surface, where O^* and OH^* were bonded, were obtained as $+1.12 e$ for CuCo_5O_8 and $+0.85 e$ for CuCo_5O_7 . Thus, the introduction of oxygen vacancies reduced the oxidation state of Co by modifying the electronic structure and was expected to affect the adsorption intensity of oxygen intermediates by less oxidizing than cobalt in CuCo_5O_8 . The stronger adsorption of oxygen intermediates on the surface of CuCo_5O_7 (110) resulted in higher OER activity.

To compare the thermodynamics-determined electrochemical potential for spontaneous reactions and understand the mechanism of catalytic O_2 production, we constructed free energy diagrams after depositing oxygen intermediates on CuCo_5O_8 (110) and CuCo_5O_7 (110), as shown in Fig. 5(a, b).

For the above-designed models, four reaction paths were considered (Eqs. (5)–(8)):



The relative free energy changes (ΔG) for oxygen intermediates were calculated as follows (Eq. (9)):

$$\Delta G = \Delta E + \Delta \text{ZPE} + T\Delta S \quad (9)$$

where ΔE is the DFT-calculated difference in ground-state energy, ΔZPE is the zero-point energy difference, and ΔS is the entropy difference. ΔZPE for each intermediate was corrected using the thermodynamic parameter table reported by Nørskov et al [60]. Potentials at pH 14 were referenced to the reversible hydrogen electrode (RHE) by shifting the electronic chemical potential according to Nernst's law. The reversible potentials (U^*) for the above steps were derived as follows (Eqs. (10)–(13), see our previous works for details [61,62]):

$$\Delta G_1 = \Delta G_{\text{OH}^*} - \Delta G_{\text{H}_2\text{O},\text{l}} + \frac{1}{2}\Delta G_{\text{H}_2} + kT \ln a_{\text{H}^+} - eU_1^0 \quad (10)$$

$$\Delta G_2 = \Delta G_{\text{O}^*} - \Delta G_{\text{OH}^*} + \frac{1}{2}\Delta G_{\text{H}_2} + kT \ln a_{\text{H}^+} - eU_2^0 \quad (11)$$

$$\Delta G_3 = \Delta G_{\text{OOH}^*} - \Delta G_{\text{O}^*} - \Delta G_{\text{H}_2\text{O}} + \frac{1}{2}\Delta G_{\text{H}_2} + kT \ln a_{\text{H}^+} - eU_3^0 \quad (12)$$

$$\Delta G_4 = \Delta G_{\text{O}_{2,\text{g}}} - \Delta G_{\text{OOH}^*} + \frac{1}{2}\Delta G_{\text{H}_2} + kT \ln a_{\text{H}^+} - eU_4^0 \quad (13)$$

where ΔG_i is the free energy difference for O^* , OH^* , OOH^* , or O^*OH^* .

According to the Sabatier principle, used to understand the kinetics of reactions where the relative adsorption energies of reaction intermediates govern catalytic activity, the catalyst-reactant interaction energy should be neither too strong nor too weak [34,61,63]. Fig. 5(c, d) presents the free energy differences for all OER steps on CuCo_5O_8 (110) and CuCo_5O_7 (110), with reversible electronic chemical potentials denoted by black ($U = 0$), blue ($U = 1.228 \text{ V}$), and red (exothermic reversible electrode potential) lines. The exothermic OER reaction potential on CuCo_5O_8 (110) was obtained as 1.760 V vs. RHE, showing a downhill shape in Fig. 5c. Remarkably, the electronic

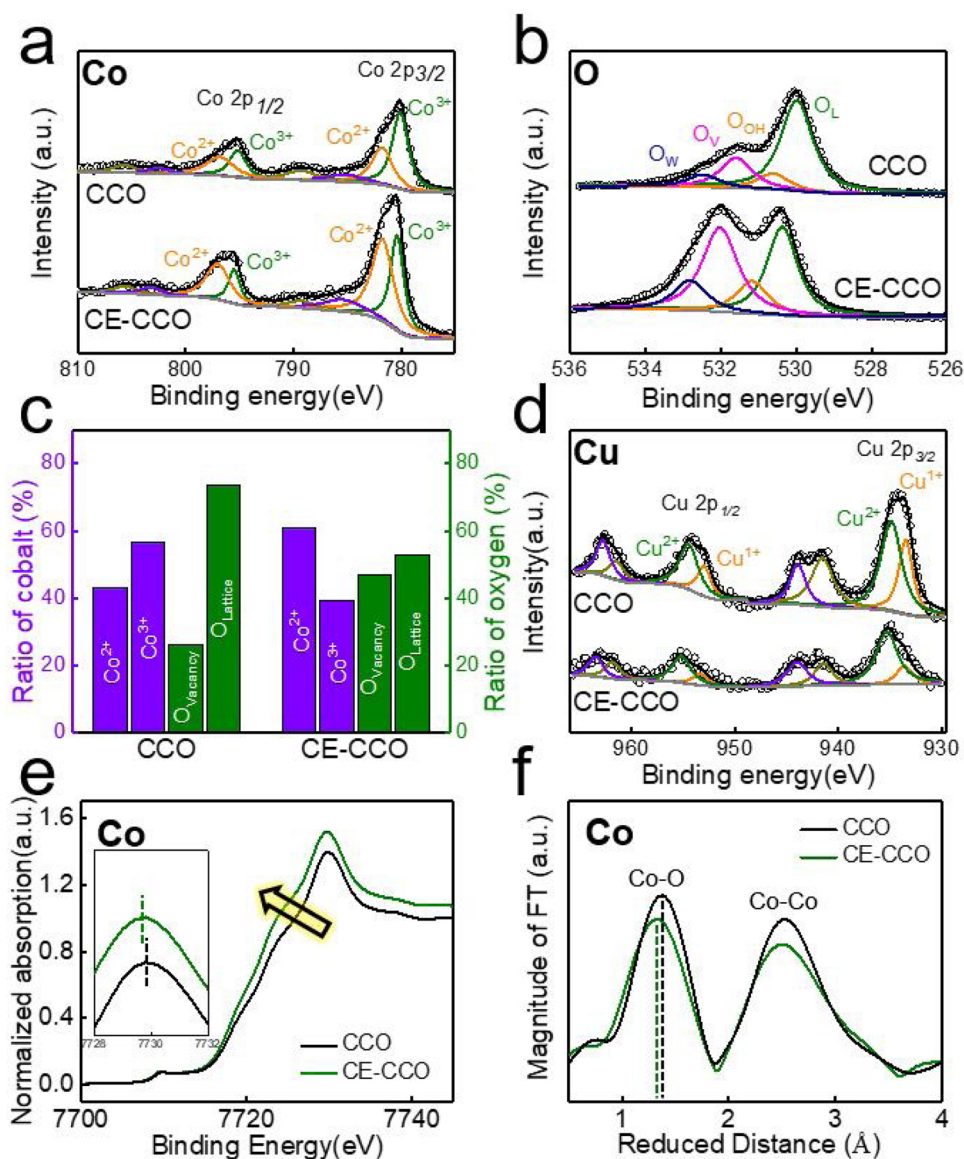


Fig. 3. Investigation of the electronic structure of the CCO and CE-CCO anode. X-ray photoelectron spectra of Co 2p (a), O 1s (b) and Cu 2p (c). (d) The Ratio of Co ([Co²⁺] and [Co³⁺]) and O ([O_{Vacancy}] and [O_{Lattice}]) was calculated from XPS results by using integral area of each element. (e) XANES spectra recorded at the Co K-edge of CCO and CE-CCO. (f) Fourier transforms (FT) of EXAFS spectra collected at Co K-edge of CCO and CE-CCO.

potential on vacancy-containing CuCo₅O₇ (110) was lower (1.498 V) than that of CuCo₅O₈ (110), indicating that lower overpotentials correspond to better OER activity. The RDSs for CuCo₅O₈ (110) and CuCo₅O₇ (110) corresponded to Eqs. (5) and (7), respectively. In the case of vacancy-free CuCo₅O₈ (110), O*OH* bonding on the surface was very difficult and thus acted a bottleneck for O₂ production. On the other hand, the removal of oxygen from the bulk lattice facilitated O*OH* bonding, and the RDS changed to OH* formation (Eq. (5)). These results explained why the presence of oxygen vacancies in the CuCoO lattice leads to better OER catalytic activity, revealing that these (etching-generated) vacancies change the electronic structure of Cu and Co to facilitate the adsorption/desorption of oxygen intermediates on/from the catalyst surface.

To confirm the practical full cell performance, we assembled an AEMWE system (Fig. 6a) comprising a current collector (stainless plate), electrolyte solution (1 M KOH) in-/outlet, gas diffusion layers (NF), and an MEA identical to that of fuel cell systems and containing an anion-exchange membrane (AEM) and hydrogen evolution reaction (HER)/OER electrodes. CE-CCO was used as the anode and Pt/C was used as the cathode. As raw NF had a rough surface, CE-CCO was

electrodeposited on pressed NF to prevent membrane physical damage. The electrolyte temperature was held constant at 45 °C.

Although AEMWE performance could be improved by increasing temperature because of the concomitant improvement of ion conductivity, mass transportation, and electrode kinetics, the corrosive environment created at overly high temperatures accelerated AEM degradation. Therefore, the constructed system was operated at a relatively low temperature [7,64]. Fig. 6b shows the linear voltammetry curves of AEMWE systems between 1.4 and 1.9 V_{cell}. As the ultimate goal of the development of a water electrolysis catalyst is its application in commercial devices, no iR compensation was performed to observe performance under real operation conditions. The operation of AEMWE could be seen in a video in supporting information. The CE-CCO AEMWE system exhibited high OER activity in the high cell voltage region (≥ 1.8 V_{cell}). The Pt/C || CE-CCO (cathode || anode) system had a lower overpotential than the Pt/C || IrO₂ one (1390 and 900 mA/cm² at 1.8 V_{cell}, respectively). Fig. 6c shows iR-corrected Tafel plots for Pt/C || IrO₂ and Pt/C || CE-CCO systems, revealing that similar Tafel slopes of ~130 mV/dec were obtained in both cases. However, it is unreasonable to compare the Tafel slope of these systems with those

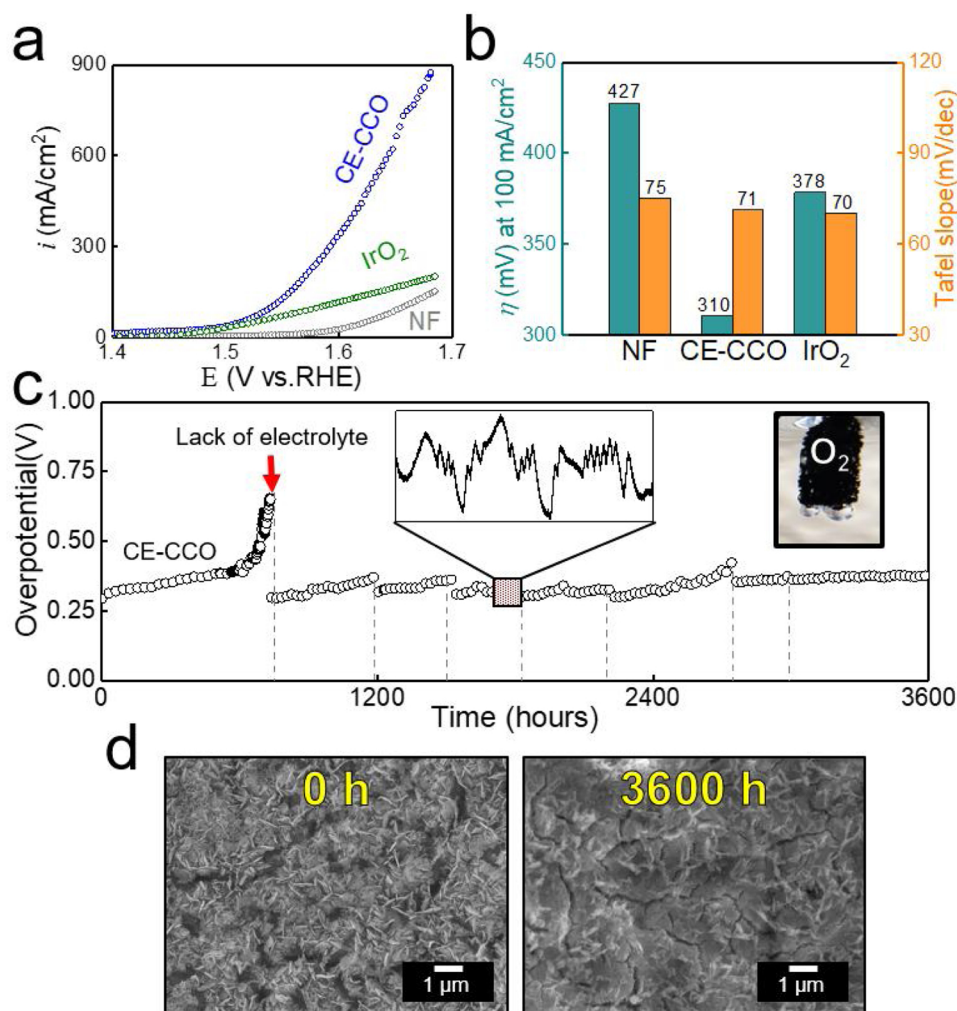


Fig. 4. Electrochemical characterization of CE-CCO anode for OER in 1 M KOH. (a) Linear sweep voltammograms (85 % iR-compensated) of the CE-CCO (blue line), commercial IrO₂ (green line) and commercial nickel foam (grey line). (b) Comparison of the overpotential at 100 mA/cm² and Tafel slope for OER obtained from LSV. (c) Durability tests of CE-CCO at 20 mA/cm² for 3600 h. (d) Scanning electron microscopy (SEM) image of surface morphology for CE-CCO before/after durability test. (For interpretation of the references to colour in this figure legend, the reader is referred to the web version of this article.)

reported in literature. Although the OER/HER mechanisms and Tafel slopes are established to some extent under acidic conditions, the corresponding mechanisms operating under alkaline conditions remain underexplored and controversial, which complicates meaningful data comparison and highlights the need for further mechanistic investigations of AEMWE systems [9,65]. Fig. 6c shows that a significant deviation from the Tafel line (dot line in Fig. 6c) was observed for Pt/C || IrO₂ with increasing cell voltage. To understand the reason for this phenomenon, the total overpotential (η_{total}) was divided into η_{ohm} , η_{kin} , and η_{mass} , as shown in Fig. 7a [1,66]. At an AEMWE current density of 200 mA/cm², Pt/C || IrO₂ featured a lower η_{total} than Pt/C || CE-CCO. In this current density region, both total overpotentials featured negligible η_{mass} contributions. However, at higher current densities, η_{total} of Pt/C || IrO₂ exceeded that of Pt/C || CE-CCO, largely because of the increase in η_{mass} . Even at a current density of 1200 mA/cm², η_{mass} of Pt/C || IrO₂ accounted for 35.4 % of η_{total} , whereas the corresponding value for Pt/C || CE-CCO was as small as 10.4 %. Although Pt/C || IrO₂ showed better performance than Pt/C || CE-CCO at low current densities, high mass transfer losses (η_{mass}) resulted in performance reversal at high current densities. This phenomenon was ascribed to the high density of catalyst layers and the presence of a polymeric binder-containing IrO₂ anode. Dense catalyst layers restricted electrolyte passage through the OER electrode and thus interfered with the smooth supply of the electrolyte [33]. On the other hand, CE-CCO was deposited as a thin layer directly

on the porous (i.e., permeable to the electrolyte) NF. The rate of oxygen gas removal from the electrode surface is another key factor influencing overall performance, as the active sites are blocked if the generated oxygen gas is not easily desorbed. In order for oxygen gas desorption to be facile, the electrode surface must have a weak affinity to this gas, i.e., needs to be aerophobic [67]. Herein, electrode aerophobicity was probed by wettability measurements, as surface aerophobicity is positively correlated with hydrophilicity [68]. The surface of the CE-CCO electrode was super-hydrophilic, i.e., superaerophobic, and that of the IrO₂/binder electrode was hydrophobic, i.e., aerophilic (Fig. 7b). In addition, the former electrode readily absorbed liquid brought in contact with its surface, whereas the latter electrode did not (Figs. 7b and S13). This phenomenon was an important clue explaining why the Pt/C || CE-CCO system had a low η_{mass} . As CE-CCO was aerophobic, the generated oxygen gas was easily desorbed from the electrode surface, which allowed the facile supply of new reactants thereto. Therefore, especially in the high current density region characterized by violent gas generation, CE-CCO showed excellent performance.

In view of the fact that industrial water electrolyzers are operated at high current densities (≥ 500 mA/cm²), the reduction of mass transfer losses is a task of high importance. In this respect, the Pt/C || CE-CCO electrode electrodeposited on NF is ideal for practical application in commercial water electrolyzers, additionally featuring the highest performance among all currently reported electrodes (Fig. 8)

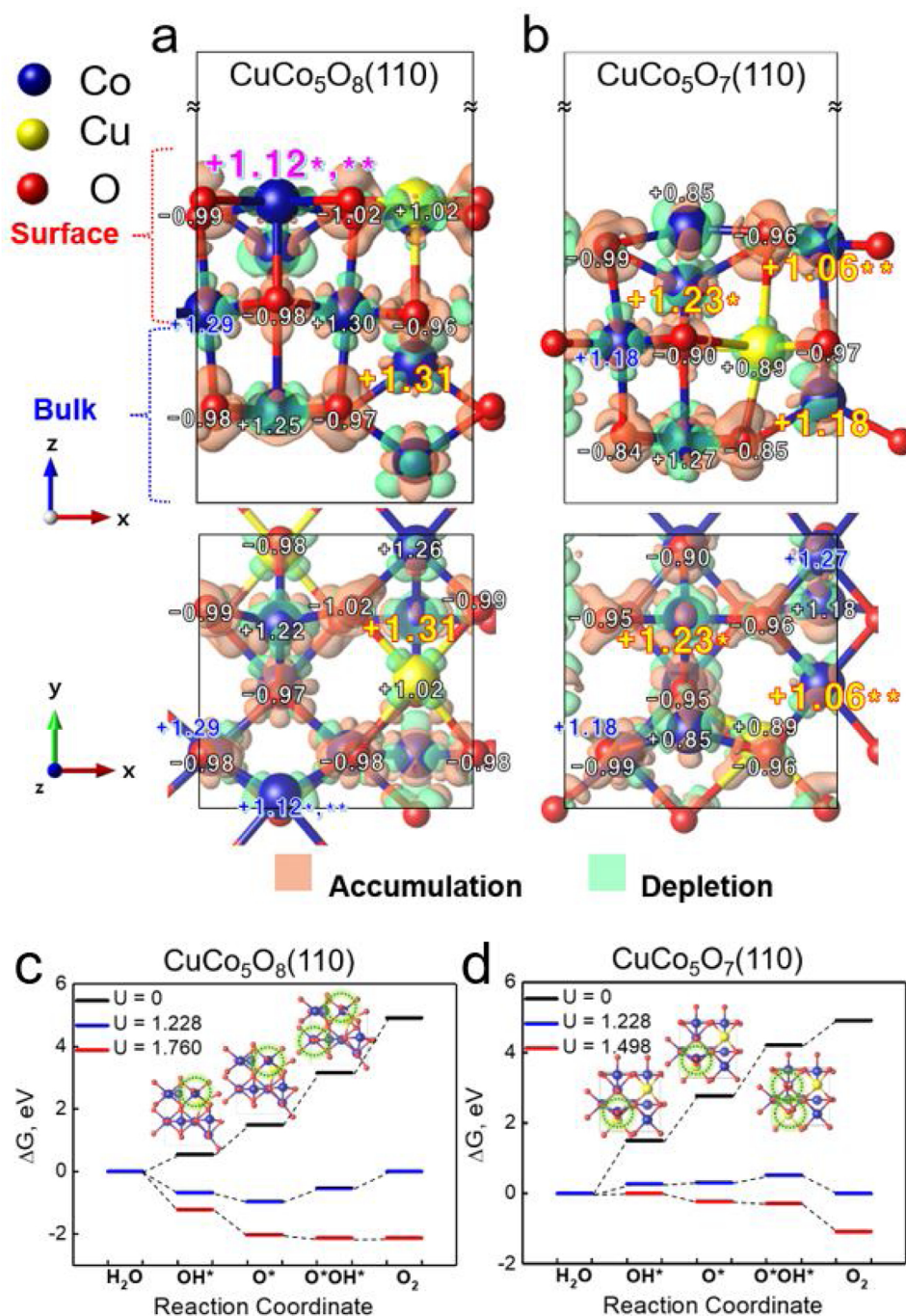


Fig. 5. Bader charge density of (a) CuCo₅O₈ (110) and (b) CuCo₅O₇ (110). * and ** are adsorption sites of O* and OH*. Standard free energy diagrams on (c) CuCo₅O₈ (110) and (d) CuCo₅O₇ (110) for OER obtained at zero potential (U = 0), and at the potential for which all step proceed downward at pH 14 and T = 298 K.

[7,9,22,26–28,55,69–80]. The superior performance of AEMWE in this study is considered to be due to electrodeposited electrode unlike the previous study. Although the results of previous studies evaluating the performance in AEMWE using CCO as a electrocatalyst for OER were relatively reported, all electrode were fabricated by spray or decal method [9,22,55,69,78–80]. This method increases the cell resistance because it uses a binder with poor electrical conductivity. In addition, since an electrode having a dense catalyst layer is used, the mass transfer resistance in the high current region is increased. The durability of the fabricated AEMWE systems was tested by 64 h application of high current density (500 mA/cm²) to single cells (Fig. 6d). The AEMWE containing CE-CCO showed good durability, featuring an initial overpotential of 1.66 V_{cell} that gradually increased to 1.74 V_{cell},

which corresponded to the retention of 82 % of the initial performance. For comparison of durability, the anode electrode for AEMWE was prepared using IrO₂ electrocatalyst (Fig. S14). When this electrode was applied under the same test conditions, the cell voltage (V_{cell}) increased by 0.38 V_{cell} compared to the initial value which showed poor durability than that of CE-CCO. In addition, the produced hydrogen gas volume was measured in real time during the durability test. The amount of hydrogen gas was 14.2 mL/min, which was constant during the durability test. The initial efficiency was 83 %, and only 4% of efficiency loss was observed during the durability test. These results indicate that the CE-CCO anode can be applied to commercialized AEMWE.

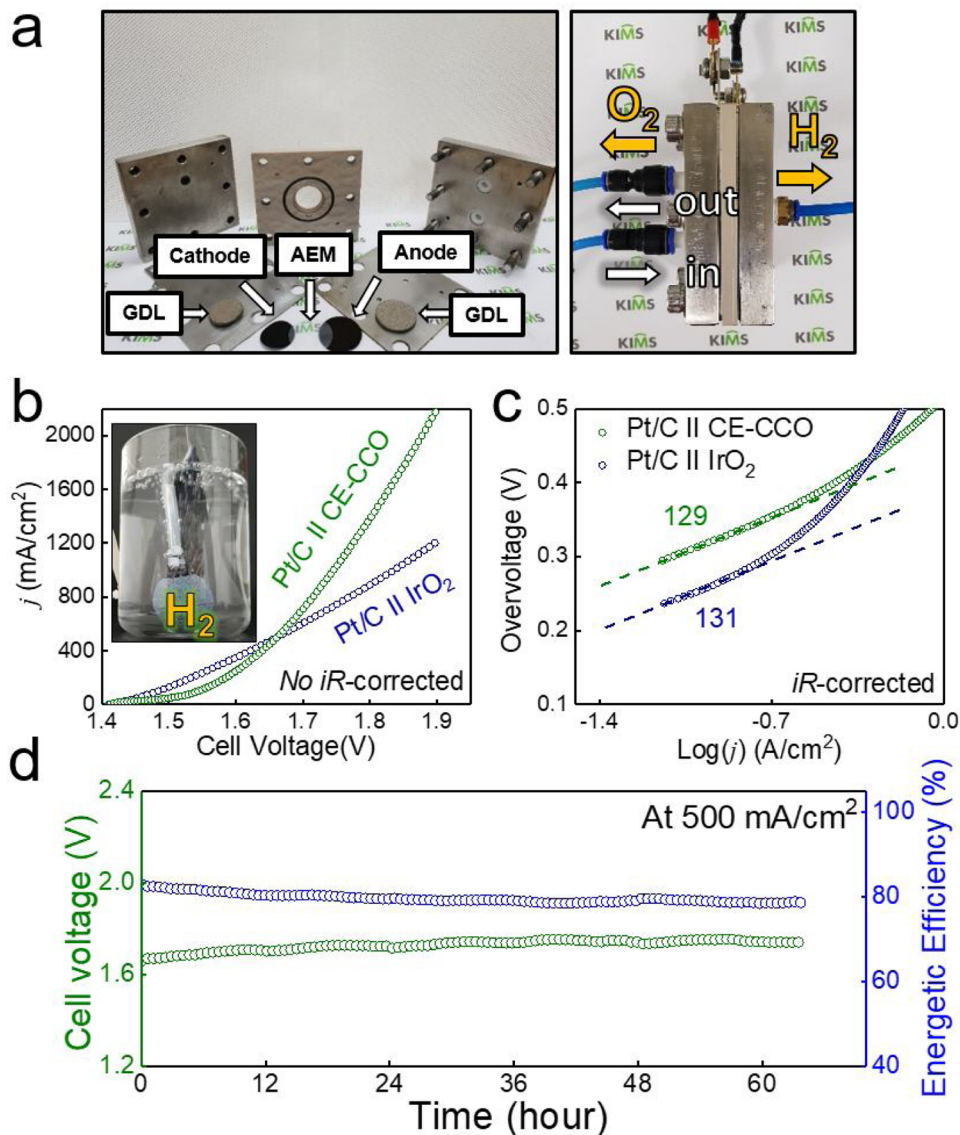


Fig. 6. Anion exchange membrane water electrolyzer (AEMWE) performance. (a) Photograph of the AEMWE configuration. The configuration of MEA is as follows: gas diffusion layer (GDL) || cathode (Pt/C) || AEM || anode (IrO₂ and CE-CCO) || GDL. The electrolyte is supplied to the anode, the anode is wet electrode and the cathode is dry electrode. (b) The polarization curves (without iR-correction) of AEMWE (Pt/C || IrO₂ and Pt/C || CE-CCO) in 1 M KOH at 45 °C. The inset image in (b) is evolved hydrogen bubbles from the cathode part (the following is the ESI related to this article Video S1). (c) Tafel plots of polarization curves for a AEMWE with an Pt/C || IrO₂ and Pt/C || CE-CCO. (d) The durability voltage-time plots for the AEMWE at 500 mA/cm² during 64 h in 1 M KOH at 45 °C.

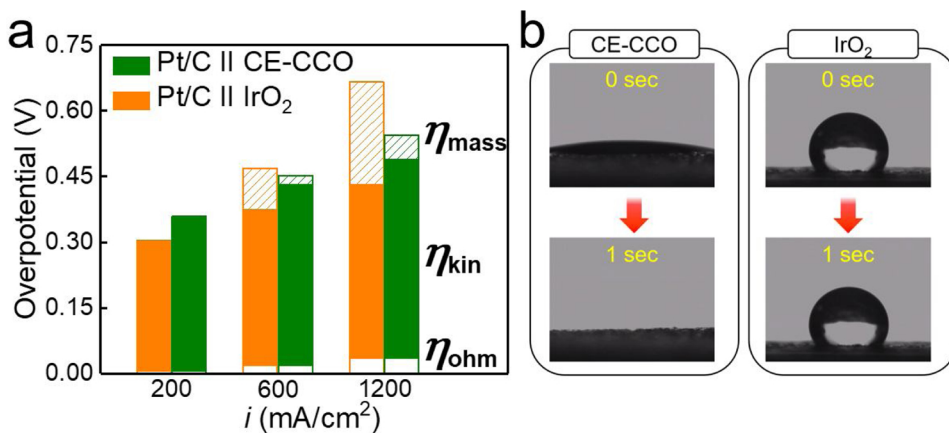


Fig. 7. Overvoltage subdivision of AEMWE. (a) The overvoltage of AEMWE was subdivided into ohmic overvoltage (η_{ohm}), kinetic overvoltage (η_{kin}) and mass-transfer overvoltage (η_{mass}) at low, mid and high current density region. (b) The wettability of the IrO₂ and CE-CCO anode was observed by distilled water on the electrode surface.

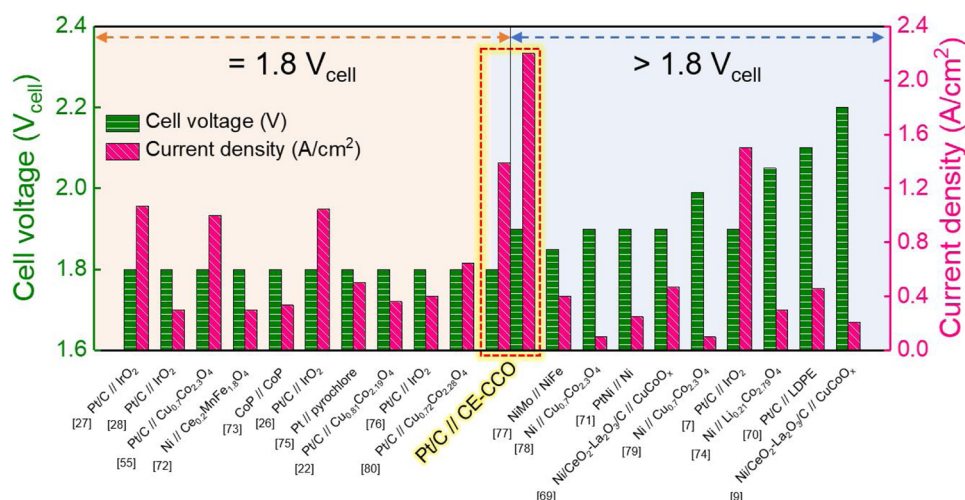


Fig. 8. Comparison of current density at 1.8 V_{cell} and above 1.8 V_{cell} as-prepared electrodes and other reported electrodes to drive AEMWE system.

4. Conclusion

A chemical etching-based method of introducing oxygen defects into CCO was developed and used to prepare an electrocatalyst for the OER under alkaline conditions. Despite the decrease in electrochemical surface area due to etching, the chemically etched CCO exhibited enhanced OER performance and remarkable durability (>3600 h) due to the changed electronic structure of Cu and Co. The above material was directly used as the anode of an AEMWE full cell, which featured high performance (1390 mA/cm² at 1.8 V_{cell}), especially at high current density, attributable to very low mass transfer resistance.

Author Contributions

Yoo Sei Park and Juchan Yang wrote the draft publication and maintained the lead position in research. Yoo Sei Park, Woo-sung Choi synthesized the electrocatalysts and evaluated their electrochemical properties. Jongmin Lee and Min Ho Seo conducted the DFT calculations. Yoo Sei Park and Juchan Yang performed the AEMWE test. Jaehoon Jeong and Myeong Je Jang assisted the physical characterizations. Juchan Yang, Yangdo Kim and Yadong Yin interpreted the XPS and XAFS. Min Ho Seo, Zhongwei Chen and Sung Mook Choi supervised this research and improved the concept of research and setting up experiments.

Declaration of Competing Interest

The authors declare that they have no known competing financial interests or personal relationships that could have appeared to influence the work reported in this paper.

Acknowledgements

This research was supported by the Fundamental Research Program of the KIMS (PNK6680 & PNK7280) & the New & Renewable Energy Core Technology Program of the KETEP (KETEP-20173010032080) & Development Program of KIER (C0-2405) in the Republic of Korea.

Appendix A. Supplementary data

Supplementary material related to this article can be found, in the online version, at doi:<https://doi.org/10.1016/j.apcatb.2020.119276>.

References

- [1] S. Choe, B.-S. Lee, M.K. Cho, H.-J. Kim, D. Henkensmeier, S.J. Yoo, J.Y. Kim, S.Y. Lee, H.S. Park, J.H. Jang, Electrodeposited IrO₂/Ti electrodes as durable and cost-effective anodes in high-temperature polymer-membrane-electrolyte water electrolyzers, *Appl. Catal. B: Environ.* 226 (2018) 289–294.
- [2] S. Siracusanu, V. Baglio, N. Van Dijk, L. Merlo, A.S. Aricò, Enhanced performance and durability of low catalyst loading PEM water electrolyser based on a short-side chain perfluorosulfonic ionomer, *Appl. Energy* 192 (2017) 477–489.
- [3] M. Bodner, A. Hofer, V. Hacker, H₂ generation from alkaline electrolyzer, *WIREs Energy Environ.* 4 (2015) 365–381.
- [4] P. Haug, B. Kreitz, M. Koj, T. Turek, Process modelling of an alkaline water electrolyzer, *Int. J. Hydrogen Energy* 42 (2017) 15689–15707.
- [5] C. Hu, L. Zhang, J. Gong, Recent progress made in the mechanism comprehension and design of electrocatalysts for alkaline water splitting, *Energy Environ. Sci.* 12 (2019) 2620–2645.
- [6] Y. Matsumoto, E. Sato, Electrocatalytic properties of transition metal oxides for oxygen evolution reaction, *Mater. Chem. Phys.* 14 (1986) 397–426.
- [7] J.E. Park, S.Y. Kang, S.-H. Oh, J.K. Kim, M.S. Lim, C.-Y. Ahn, Y.-H. Cho, Y.-E. Sung, High-performance anion-exchange membrane water electrolysis, *Electrochim. Acta* 295 (2019) 99–106.
- [8] D. Xu, M.B. Stevens, M.R. Cosby, S.Z. Oener, A.M. Smith, L.J. Enman, K.E. Ayers, C.B. Capuano, J.N. Renner, N. Danilovic, Y. Li, H. Wang, Q. Zhang, S.W. Boettcher, Earth-abundant oxygen electrocatalysts for alkaline anion-exchange-membrane water electrolysis: effects of catalyst conductivity and comparison with performance in three-electrode cells, *ACS Catal.* 9 (2019) 7–15.
- [9] C.C. Pavel, F. Ceccconi, C. Emiliani, S. Santicioli, A. Scaffidi, S. Catanorchi, M. Comotti, Highly efficient platinum group metal free based membrane-electrode assembly for anion exchange membrane water electrolysis, *Angew. Chem. Int. Ed.* 53 (2014) 1378–1381.
- [10] Y.S. Park, J.H. Lee, M.J. Jang, J. Jeong, S.M. Park, W.-S. Choi, Y. Kim, J. Yang, S.M. Choi, Co₃S₄ nanosheets on Ni foam via electrodeposition with sulfurization as highly active electrocatalysts for anion exchange membrane electrolyzer, *Int. J. Hydrogen Energy* (2019).
- [11] F. Yu, H. Zhou, Y. Huang, J. Sun, F. Qin, J. Bao, W.A. Goddard, S. Chen, Z. Ren, High-performance bifunctional porous non-noble metal phosphide catalyst for overall water splitting, *Nat. Commun.* 9 (2018) 2551.
- [12] H. Zhou, F. Yu, Q. Zhu, J. Sun, F. Qin, L. Yu, J. Bao, Y. Yu, S. Chen, Z. Ren, Water splitting by electrolysis at high current densities under 1.6 volts, *Energy Environ. Sci.* 11 (2018) 2858–2864.
- [13] T.J. Meyer, The art of splitting water, *Nature* 451 (2008) 778–779.
- [14] J. Jiang, S. Lu, W.-K. Wang, G.-X. Huang, B.-C. Huang, F. Zhang, Y.-J. Zhang, H.-Q. Yu, Ultrahigh electrocatalytic oxygen evolution by iron-nickel sulfide nanosheets/reduced graphene oxide nano-hybrids with an optimized autoxidation process, *Nano Energy* 43 (2018) 300–309.
- [15] H.Q. Fu, L. Zhang, C.W. Wang, L.R. Zheng, P.F. Liu, H.G. Yang, 1D/1D hierarchical nickel sulfide/phosphide nanostructures for electrocatalytic water oxidation, *ACS Energy Lett.* 3 (2018) 2021–2029.
- [16] H. Xu, J. Cao, C. Shan, B. Wang, P. Xi, W. Liu, Y. Tang, MOF-derived hollow Co₃O₄ decorated with CeO_x nanoparticles for boosting oxygen evolution reaction electrocatalysis, *Angew. Chem. Int. Ed.* 57 (2018) 8654–8658.
- [17] Y.-R. Hong, S. Mhin, K.-M. Kim, W.-S. Han, H. Choi, G. Ali, K.Y. Chung, H.J. Lee, S.-I. Moon, S. Dutta, S. Sun, Y.-G. Jung, T. Song, H. Han, Electrochemically activated cobalt nickel sulfide for an efficient oxygen evolution reaction: partial amorphization and phase control, *J. Mater. Chem. A* 7 (2019) 3592–3602.
- [18] Z. Xiao, Y. Wang, Y.-C. Huang, Z. Wei, C.-L. Dong, J. Ma, S. Shen, Y. Li, S. Wang, Filling the oxygen vacancies in Co₃O₄ with phosphorus: an ultra-efficient electrocatalyst for overall water splitting, *Energy Environ. Sci.* 10 (2017) 2563–2569.

- [19] J. Sanchez, T.R. Hellstern, L.A. King, T.F. Jaramillo, Surface engineering of 3D gas diffusion electrodes for high-performance H₂ production with nonprecious metal catalysts, *Adv. Energy Mater.* 9 (2019) 1901824.
- [20] P. Zhang, L. Li, D. Nordlund, H. Chen, L. Fan, B. Zhang, X. Sheng, Q. Daniel, L. Sun, Dendritic core-shell nickel-iron-copper metal/metal oxide electrode for efficient electrocatalytic water oxidation, *Nat. Commun.* 9 (2018) 381.
- [21] W. Xu, F. Lyu, Y. Bai, A. Gao, J. Feng, Z. Cai, Y. Yin, Porous cobalt oxide nanoplates enriched with oxygen vacancies for oxygen evolution reaction, *Nano Energy* 43 (2018) 110–116.
- [22] W.-S. Choi, M.J. Jang, Y.S. Park, K.H. Lee, J.Y. Lee, M.-H. Seo, S.M. Choi, Three-dimensional honeycomb-like Cu_{0.81}Co_{2.19}O₄ nanosheet arrays supported by Ni foam and their high efficiency as oxygen evolution electrodes, *ACS Appl. Mater. Interfaces* 10 (2018) 38663–38668.
- [23] Q. Zhou, Y. Chen, G. Zhao, Y. Lin, Z. Yu, X. Xu, X. Wang, H.K. Liu, W. Sun, S.X. Dou, Active-site-enriched iron-doped nickel/cobalt hydroxide nanosheets for enhanced oxygen evolution reaction, *ACS Catal.* 8 (2018) 5382–5390.
- [24] Y. Yang, L. Dang, M.J. Shearer, H. Sheng, W. Li, J. Chen, P. Xiao, Y. Zhang, R.J. Hamers, S. Jin, Highly active trimetallic NiFeCr layered double hydroxide electrocatalysts for oxygen evolution reaction, *Adv. Energy Mater.* 8 (2018) 1703189.
- [25] C. Kuai, Y. Zhang, D. Wu, D. Sokaras, L. Mu, S. Spence, D. Nordlund, F. Lin, X.-W. Du, Fully oxidized Ni-Fe layered double hydroxide with 100% exposed active sites for catalyzing oxygen evolution reaction, *ACS Catal.* 9 (2019) 6027–6032.
- [26] A. Lim, H.-j. Kim, D. Henkensmeier, S. Jong Yoo, J. Young Kim, S. Young Lee, Y.-E. Sung, J.H. Jang, H.S. Park, A study on electrode fabrication and operation variables affecting the performance of anion exchange membrane water electrolysis, *J. Ind. Eng. Chem.* 76 (2019) 410–418.
- [27] M.K. Cho, H.-Y. Park, H.J. Lee, H.-J. Kim, A. Lim, D. Henkensmeier, S.J. Yoo, J.Y. Kim, S.Y. Lee, H.S. Park, J.H. Jang, Alkaline anion exchange membrane water electrolysis: effects of electrolyte feed method and electrode binder content, *J. Power Sources* 382 (2018) 22–29.
- [28] M.K. Cho, H.-Y. Park, S. Choe, S.J. Yoo, J.Y. Kim, H.-J. Kim, D. Henkensmeier, S.Y. Lee, Y.-E. Sung, H.S. Park, J.H. Jang, Factors in electrode fabrication for performance enhancement of anion exchange membrane water electrolysis, *J. Power Sources* 347 (2017) 283–290.
- [29] X. Lu, C. Zhao, Electrodeposition of hierarchically structured three-dimensional nickel-iron electrodes for efficient oxygen evolution at high current densities, *Nat. Commun.* 6 (2015) 6616.
- [30] J. Lobato, P. Cañizares, M.A. Rodrigo, C. Ruiz-López, J.J. Linares, Influence of the Teflon loading in the gas diffusion layer of PBI-based PEM fuel cells, *J. Appl. Electrochem.* 38 (2008) 793–802.
- [31] E. Antolini, A. Pozio, L. Giorgi, E. Passalacqua, Morphological characteristics of carbon/polytetrafluoroethylene films deposited on porous carbon support, *J. Mater. Sci.* 33 (1998) 1837–1843.
- [32] Y.S. Park, W.-S. Choi, M.J. Jang, J.H. Lee, S. Park, H. Jin, M.H. Seo, K.-H. Lee, Y. Yin, Y. Kim, J. Yang, S.M. Choi, Three-dimensional dendritic Cu-Co-P electrode by one-step electrodeposition on a hydrogen bubble template for hydrogen evolution reaction, *ACS Sustain. Chem. Eng.* 7 (2019) 10734–10741.
- [33] J.H. Kim, J. Kim, H. Kim, J. Kim, S.H. Ahn, Facile fabrication of nanostructured NiMo cathode for high-performance proton exchange membrane water electrolyzer, *J. Ind. Eng. Chem.* 79 (2019) 255–260.
- [34] G. Kresse, J. Furthmüller, Efficient iterative schemes for ab initio total-energy calculations using a plane-wave basis set, *Phys. Rev. B* 54 (1996) 11169–11186.
- [35] P.E. Blöchl, Projector augmented-wave method, *Phys. Rev. B* 50 (1994) 17953–17979.
- [36] G. Kresse, D. Joubert, From ultrasoft pseudopotentials to the projector augmented-wave method, *Phys. Rev. B* 59 (1999) 1758–1775.
- [37] B. Hammer, L.B. Hansen, J.K. Nørskov, Improved adsorption energetics within density-functional theory using revised Perdew-Burke-Ernzerhof functionals, *Phys. Rev. B* 59 (1999) 7413–7421.
- [38] G. Kresse, J. Furthmüller, Efficiency of ab-initio total energy calculations for metals and semiconductors using a plane-wave basis set, *Comput. Mater. Sci.* 6 (1996) 15–50.
- [39] G. Hautier, S.P. Ong, A. Jain, C.J. Moore, G. Ceder, Accuracy of density functional theory in predicting formation energies of ternary oxides from binary oxides and its implication on phase stability, *Phys. Rev. B* 85 (2012) 155208.
- [40] C. Franchini, R. Podloucky, J. Paier, M. Marsman, G. Kresse, Ground-state properties of multivalent manganese oxides: density functional and hybrid density functional calculations, *Phys. Rev. B* 75 (2007) 195128.
- [41] Y.-L. Lee, J. Kleis, J. Rossmeisl, D. Morgan, Ab initio energetics of LaBO₃(001) (B = Mn, Fe, Co, and Ni) for solid oxide fuel cell cathodes, *Phys. Rev. B* 80 (2009) 224101.
- [42] M. Methfessel, A.T. Paxton, High-precision sampling for Brillouin-zone integration in metals, *Phys. Rev. B* 40 (1989) 3616–3621.
- [43] K. Mathew, R. Sundaraman, K. Letchworth-Weaver, T.A. Arias, R.G. Hennig, Implicit solvation model for density-functional study of nanocrystal surfaces and reaction pathways, *J. Chem. Phys.* 140 (2014) 084106.
- [44] B. RFW, *Atoms in Molecules: A Quantum Theory*, Clarendon Press, 1994.
- [45] Q. Lu, M.W. Lattanzi, Y. Chen, X. Kou, W. Li, X. Fan, K.M. Unruh, J.G. Chen, J.Q. Xiao, Supercapacitor electrodes with high-energy and power densities prepared from monolithic NiO/Ni nanocomposites, *Angew. Chem. Int. Ed.* 50 (2011) 6847–6850.
- [46] R. Wei, M. Fang, G. Dong, C. Lan, L. Shu, H. Zhang, X. Bu, J.C. Ho, High-index faceted porous Co₃O₄ nanosheets with oxygen vacancies for highly efficient water oxidation, *ACS Appl. Mater. Interfaces* 10 (2018) 7079–7086.
- [47] H. Schäfer, D.M. Chevrier, K. Kuepper, P. Zhang, J. Wollschlaeger, D. Daum, M. Steinhart, C. Heß, U. Krupp, K. Müller-Buschbaum, J. Stangl, M. Schmidt, X₂OCoCrW₁₀Mo₁₀-9//Co₃O₄: a metal-ceramic composite with unique efficiency values for water-splitting in the neutral regime, *Energy Environ. Sci.* 9 (2016) 2609–2622.
- [48] J. Yang, S. Park, Ky. Choi, H.-S. Park, Y.-G. Cho, H. Ko, H.-K. Song, Activity-durability coincidence of oxygen evolution reaction in the presence of carbon corrosion: case study of MnCo₂O₄ spinel with carbon black, *ACS Sustain. Chem. Eng.* 6 (2018) 9566–9571.
- [49] X. Fan, M.-S. Balogun, Y. Huang, Y. Tong, Oxygen-deficient three-dimensional porous Co₃O₄ nanowires as an electrode material for water oxidation and energy storage, *ChemElectroChem* 4 (2017) 2453–2459.
- [50] H. Zhang, J. Zhang, Y. Li, H. Jiang, H. Jiang, C. Li, Continuous oxygen vacancy engineering of the Co₃O₄ layer for an enhanced alkaline electrocatalytic hydrogen evolution reaction, *J. Mater. Chem. A* 7 (2019) 13506–13510.
- [51] J. Bao, X. Zhang, B. Fan, J. Zhang, M. Zhou, W. Yang, X. Hu, H. Wang, B. Pan, Y. Xie, Ultrathin spinel-structured nanosheets rich in oxygen deficiencies for enhanced electrocatalytic water oxidation, *Angew. Chem. Int. Ed.* 54 (2015) 7399–7404.
- [52] G.B. Della Mea, L.P. Matte, A.S. Thill, F.O. Lobato, E.V. Benvenuti, L.T. Arenas, A. Jürgensen, R. Hergenröder, F. Poletto, F. Bernardi, Tuning the oxygen vacancy population of cerium oxide (CeO_{2-x}, 0 < x < 0.5) nanoparticles, *Appl. Surf. Sci.* 422 (2017) 1102–1112.
- [53] S. Gao, Z. Sun, W. Liu, X. Jiao, X. Zu, Q. Hu, Y. Sun, T. Yao, W. Zhang, S. Wei, Y. Xie, Atomic layer confined vacancies for atomic-level insights into carbon dioxide electroreduction, *Nat. Commun.* 8 (2017) 14503.
- [54] J. Park, Y.J. Sa, H. Baik, T. Kwon, S.H. Joo, K. Lee, Iridium-based multimetallic Nanoframe@Nanoframe structure: an efficient and robust electrocatalyst toward oxygen evolution reaction, *ACS Nano* 11 (2017) 5500–5509.
- [55] X. Wu, K. Scott, CuxCo_{3-x}O₄ (0 ≤ x < 1) nanoparticles for oxygen evolution in high performance alkaline exchange membrane water electrolyzers, *J. Mater. Chem. C* 21 (2011) 12344–12351.
- [56] C.C.L. McCrory, S. Jung, J.C. Peters, T.F. Jaramillo, Benchmarking heterogeneous electrocatalysts for the oxygen evolution reaction, *J. Am. Chem. Soc.* 135 (2013) 16977–16987.
- [57] A. Belsky, M. Hellenbrandt, V.L. Karen, P. Luksch, New developments in the Inorganic Crystal Structure Database (ICSD): accessibility in support of materials research and design, *Acta Crystallogr. Sect. B* 58 (2002) 364–369.
- [58] B.C. Han, A. Van der Ven, G. Ceder, B.-J. Hwang, Surface segregation and ordering of alloy surfaces in the presence of adsorbates, *Phys. Rev. B* 72 (2005) 205409.
- [59] M.H. Seo, S.M. Choi, E.J. Lim, I.H. Kwon, J.K. Seo, S.H. Noh, W.B. Kim, B. Han, Toward new fuel cell support materials: a theoretical and experimental study of nitrogen-doped graphene, *ChemSusChem* 7 (2014) 2609–2620.
- [60] J.K. Nørskov, J. Rossmeisl, A. Logadottir, L. Lindqvist, J.R. Kitchin, T. Bligaard, H. Jónsson, Origin of the overpotential for oxygen reduction at a fuel-cell cathode, *J. Phys. Chem. B* 108 (2004) 17886–17892.
- [61] M.H. Seo, H.W. Park, D.U. Lee, M.G. Park, Z. Chen, Design of highly active perovskite oxides for oxygen evolution reaction by combining experimental and ab initio studies, *ACS Catal.* 5 (2015) 4337–4344.
- [62] S.H. Noh, C. Kwon, J. Hwang, T. Ohsaka, B.-J. Kim, T.-Y. Kim, Y.-G. Yoon, Z. Chen, M.H. Seo, B. Han, Self-assembled nitrogen-doped fullerenes and their catalysis for fuel cell and rechargeable metal-air battery applications, *Nanoscale* 9 (2017) 7373–7379.
- [63] J. Greeley, I.E.L. Stephens, A.S. Bondarenko, T.P. Johansson, H.A. Hansen, T.F. Jaramillo, J. Rossmeisl, I. Chorkendorff, J.K. Nørskov, Alloys of platinum and early transition metals as oxygen reduction electrocatalysts, *Nat. Chem.* 1 (2009) 552–556.
- [64] A. Lim, M.K. Cho, S.Y. Lee, H.-J. Kim, S.J. Yoo, Y.-E. Sung, J.H. Jang, H.S. Park, A review of industrially developed components and operation conditions for anion exchange membrane water electrolysis, *J. Electrochem. Sci. Technol.* 8 (2017) 265–273.
- [65] I.V. Pushkareva, A.S. Pushkarev, S.A. Grigoriev, P. Modisha, D.G. Bessarabov, Comparative study of anion exchange membranes for low-cost water electrolysis, *Int. J. Hydrogen Energy* (2019).
- [66] H. Kim, S. Choe, H. Park, J.H. Jang, S.H. Ahn, S.-K. Kim, An extremely low Pt loading cathode for a highly efficient proton exchange membrane water electrolyzer, *Nanoscale* 9 (2017) 19045–19049.
- [67] M. Jiang, H. Wang, Y. Li, H. Zhang, G. Zhang, Z. Lu, X. Sun, L. Jiang, Superaerophobic RuO₂-based nanostructured electrode for high-performance chlorine evolution reaction, *Small* 13 (2017) 1602240.
- [68] J.E. George, S. Chidangil, S.D. George, Recent progress in fabricating super-aerophobic and superaerophilic surfaces, *Adv. Mater. Interfaces* 4 (2017) 1601088.
- [69] L. Zeng, T.S. Zhao, Integrated inorganic membrane electrode assembly with layered double hydroxides as ionic conductors for anion exchange membrane water electrolysis, *Nano Energy* 11 (2015) 110–118.
- [70] M. Faraj, M. Boccia, H. Miller, F. Martini, S. Borsacchi, M. Geppi, A. Pucci, New LDPE based anion-exchange membranes for alkaline solid polymeric electrolyte water electrolysis, *Int. J. Hydrogen Energy* 37 (2012) 14992–15002.
- [71] S.H. Ahn, S.J. Yoo, H.-J. Kim, D. Henkensmeier, S.W. Nam, S.-K. Kim, J.H. Jang, Anion exchange membrane water electrolyzer with an ultra-low loading of Pt-decorated Ni electrocatalyst, *Appl. Catal. B* 180 (2016) 674–679.
- [72] T. Pandiarajan, L. John Berchmans, S. Ravichandran, Fabrication of spinel ferrite based alkaline anion exchange membrane water electrolyzers for hydrogen production, *RSC Adv.* 5 (2015) 34100–34108.
- [73] J. Chang, L. Liang, C. Li, M. Wang, J. Ge, C. Liu, W. Xing, Ultrathin cobalt phosphide nanosheets as efficient bifunctional catalysts for a water electrolysis cell and the origin for cell performance degradation, *Green Chem.* 18 (2016) 2287–2295.

- [74] X. Wu, K. Scott, A Li-doped Co₃O₄ oxygen evolution catalyst for non-precious metal alkaline anion exchange membrane water electrolyzers, *Int. J. Hydrogen Energy* 38 (2013) 3123–3129.
- [75] J. Parrondo, M. George, C. Capuano, K.E. Ayers, V. Ramani, Pyrochlore electrocatalysts for efficient alkaline water electrolysis, *J. Mater. Chem. A* 3 (2015) 10819–10828.
- [76] Y. Leng, G. Chen, A.J. Mendoza, T.B. Tighe, M.A. Hickner, C.-Y. Wang, Solid-state water electrolysis with an alkaline membrane, *J. Am. Chem. Soc.* 134 (2012) 9054–9057.
- [77] L. Xiao, S. Zhang, J. Pan, C. Yang, M. He, L. Zhuang, J. Lu, First implementation of alkaline polymer electrolyte water electrolysis working only with pure water, *Energy Environ. Sci.* 5 (2012) 7869–7871.
- [78] X. Wu, K. Scott, A polymethacrylate-based quaternary ammonium OH[−] ionomer binder for non-precious metal alkaline anion exchange membrane water electrolyzers, *J. Power Sources* 214 (2012) 124–129.
- [79] Y.-C. Cao, X. Wu, K. Scott, A quaternary ammonium grafted poly vinyl benzyl chloride membrane for alkaline anion exchange membrane water electrolyzers with no-noble-metal catalysts, *Int. J. Hydrogen Energy* 37 (2012) 9524–9528.
- [80] S.M. Park, M.J. Jang, Y.S. Park, J. Lee, J.-y. Jeong, J. Jung, M.-K. Choi, Y.-S. Noh, M.-H. Seo, H.J. Kim, J. Yang, Y.D. Kim, S.M. Choi, Synthesis and characterization of the Cu_{0.72}Co_{2.28}O₄ catalyst for oxygen evolution reaction in an anion exchange membrane water electrolyzer, *Korean J. Met. Mater.* 58 (2020) 49–58.